

Mass Transfer Characteristics of CO₂ and Blended Aqueous Solutions of [C₂OHmim][Lys]/MDEA in a Microchannel

Zhenbin Xu, Tingting Wang, Jianmeng Wu, Lulu Wang, Xiangping Zhang, Haifeng Dong,* and Changyu Sun*



Cite This: *Ind. Eng. Chem. Res.* 2023, 62, 8926–8938



Read Online

ACCESS |

Metrics & More

Article Recommendations

Supporting Information

ABSTRACT: In this paper, the two-phase flow and mass transfer process of CO₂ and [C₂OHmim][Lys]/MDEA mixed aqueous solution in a T-shaped microchannel were investigated systematically. By using a high-speed camera connected to a computer, the two-phase flow patterns were recorded online, including the Taylor flow and a small amount of Taylor-bubbly flow. And the effects of ionic liquid concentration and two-phase flow ratio (Q_G/Q_L) on bubble length, specific surface area, gas holdup, and mass transfer coefficient were studied experimentally. The results indicate that the blended solution of [C₂OHmim][Lys]/MDEA could significantly enhance two-phase mass transfer compared to single N-methyldiethanolamine aqueous solution. The reaction mechanism between CO₂ and ionic liquid/amine mixed aqueous solution was also analyzed. On the basis of experimental data, some new correlations for predicting the bubble initial length and the volumetric mass transfer coefficient were proposed, which matched well with the experimental data. This work is helpful to provide new ideas for the design of CO₂ absorbents and further improve the data of gas–liquid mass transfer in microchannels.



1. INTRODUCTION

The greenhouse effect and global warming become more and more pronounced because of the excessive emission of industrial gases and the burning of fossil energy, which have attracted great attention from all over the world. In recent years, to tackle climate change and achieve a global green transition, China has taken strong policies and measures and proposed major strategic decisions for carbon neutrality and carbon peaking. CO₂ capture is a significant route to reduce the greenhouse effect.^{1,2} Currently, CO₂ capture technologies include chemical absorption,^{3,4} physical absorption,⁵ and membrane separation,^{6–9} among which chemical absorption is the most widely applied in the industry. The common absorbents are monoethanolamine (MEA), diethanolamine (DEA), *N*-methyldiethanolamine (MDEA), and other single alcoholic amine solutions^{10–13} or their mixed amine solutions.^{14,15} However, some inherent properties of alkylamines limit their use, such as the high volatility, higher heat of reaction, corrosion of equipment and piping, etc.¹⁶ Hence, it is very important to develop more effective, process safe, and green absorbents.

Ionic liquids are new absorbents with promising industrial applications. Most ionic liquids are liquid at or near room temperature, whose type and structure can be changed by altering the anion or cation. According to the interaction mechanism with gas, ionic liquids can be classified into

traditional and functionalized types. Traditional ionic liquids absorb CO₂ mainly by physical absorption, which have disadvantages of slow absorption rate and low absorption load, whereas functionalized ionic liquids contain special groups such as amino groups, which can react with CO₂ to generate new substances, thereby greatly improving the absorption performance. Ionic liquids have many advantages that are unmatched by traditional solvents, such as high thermal stability, low vapor pressure, adjustable physical and chemical properties, strong solubility, etc., and are considered a potential green solvent.^{17,18} However, the high viscosity and high price of ionic liquids limit their industrial application. Thus, ionic liquids and alkanolamines have been compounded by researchers to solve these problems because the hybrid solvent could improve the physical properties of the solution (viscosity, volatility, etc.), reduce the cost of absorbents, and retain the high absorption of CO₂.^{19–23} Yuan et al.²² studied the performance of [Cho][Gly]/MDEA mixed aqueous solution for CO₂ absorption under different experimental

Received: December 9, 2022

Revised: May 1, 2023

Accepted: May 16, 2023

Published: May 27, 2023



conditions, and results showed that the addition of [Cho][Gly] could increase the reactivity of MDEA. Furthermore, the mixed solution of [Cho][Gly] and MDEA with mass fractions of 10 and 20% had the best absorption and regeneration performance. Moreover, Xiao et al.²³ synthesized four traditional ionic liquids by changing the carbon chain length of imidazolium cations and compared the CO₂ absorption performance of pure ionic liquids and ionic liquids + MEA/MDEA hybrid solutions. By measuring the CO₂ absorption capacity of different solutions and the viscosity before and after absorption, the addition of amines can significantly reduce the viscosity of the mixed solvent, thereby improving the CO₂ absorption rate. The mixed solvent [BEIM][BF₄] and MDEA shows the best performance in CO₂ loading and regeneration energy consumption.

At present, large traditional chemical equipment such as packed towers is usually used for the absorption of CO₂.²⁴ However, traditional chemical equipment is bulky, with high consumption of raw materials and low mass transfer efficiency. The advent of the microchannel reactor has opened up new opportunities for the CO₂ absorption process. The micro-reactor is mainly composed of channels with a characteristic size of nanometers to micrometers, and the length of the main channel is usually a few centimeters. The shape inside the channel is diverse and complex. Researchers usually design different shapes according to experimental requirements, such as T-shaped, tree-shaped, etc. For different reaction systems, the material of microchannels is also different. At present, polymer and glass materials are widely used at the laboratory level, among which glass is more suitable for oxidizing liquid phase systems. These two substances have good optical properties and can be well applied to visualization research. Compared with the traditional reactor, the microchannel has the advantages of high specific surface area, high controllability of mass transfer process, and small volume. The gas–liquid mass transfer process can be significantly strengthened by reducing the diffusion distance and increasing the concentration gradient and the phase boundary area, which already shows promising applications in gas absorption,²⁵ organic synthesis,²⁶ and extraction.²⁷ For example, microchannels are widely used in highly exothermic reactions (such as nitration, alkylation, etc.) and other process unstable reactions. Because the microchannel can quickly realize the mass transfer and heat transfer in the channel in a short time, the heat can be exported in time. Meanwhile, the amounts of reactants operated online in the microchannel are small, which can greatly reduce the occurrence of accidents. In addition, the residence time in the microchannel is short, which can effectively avoid side reactions. Both the microchannel and another microreactor, the tube-in-tube reactor, can provide a large gas–liquid contact area and improve the gas–liquid mass transfer process. They are widely used in chemical, biological, and other fields. However, the tube-in-tube reactor needs to replace the matching membrane components for gases with different molecular sizes, and the microchannel has better universality. In addition, the microchannel can be visualized by a high-speed camera. Moreover, the microchannel is also suitable for liquid–liquid mass transfer. Finally, the microchannel structure could be changed to further improve the mass transfer performance. Several scholars have already studied the flow and mass transfer characteristics using microchannels with different sizes and shapes, providing new ideas for efficient CO₂ absorption.^{28–30} Ma et al.²⁸ applied the MEA and DEEA

hybrid solvent as continuous phase for CO₂ absorption in a T-shaped microchannel and systematically analyzed the transition mechanism of flow patterns as well as mass transfer characteristics. Bubbles would evolve into different flow patterns in the main channel due to different dominant forces. The calculated results show that the microchannel can significantly improve the mass transfer coefficient compared to a conventional column. Guo et al.²⁹ investigated the mass transfer performance in a microchannel by using AMP-EG solution to absorb CO₂. On the basis of calculation results, the mass transfer coefficient at lower AMP concentration in the microchannel is still much higher than that at higher AMP concentration in a wetted wall column. Janati et al.³⁰ carried out a study of CO₂ removal in a T-junction microchannel. During this work, CO₂ absorbents were prepared by blending MEA separately with DEA and TEA, and then they were used to absorb the mixture of CO₂ and N₂, respectively. Experimental results show that the microchannel can significantly increase the overall gas-phase mass transfer coefficient compared to other traditional contactors, which provides a new approach to obtain high absorption percentages. Furthermore, some researchers used ionic liquids as CO₂ absorbents to explore the mass transfer and flow of CO₂-ILs in microchannels. Ma et al.³¹ explored the two-phase flow and pressure drop of three different ionic liquid aqueous solutions absorbing CO₂ in microchannels. The results show that the functionalized ionic liquids ([Apmim][BF₄]) that can chemically react with CO₂ have the best absorption performance compared to the other two ionic liquids ([OHemim][BF₄], [Bmim][CH₃SO₄]) that physically absorb CO₂. In addition, Zhang et al.³² studied the mass transfer of CO₂ and conventional ionic liquid ([Bmim][BF₄])/ethanol mixed solution in microchannels and investigated the influence of the two-phase flow ratio and ionic liquid concentration on the mass transfer coefficient. At present, most studies focus on the absorption of CO₂ in microchannels using a single ionic liquid aqueous solution. Among them, conventional ionic liquids are more popular for experimental continuous phase. However, there are few studies on the CO₂ absorption into a functionalized ionic liquid/alkanolamine mixed aqueous solution in the microchannel and the explanation of the reaction mechanism. Yin et al.³³ used the complex solutions of [C₂OHmim][Gly] and amine as absorbents to explore the two-phase mass transfer process in microchannels. According to the relevant literature,^{34,35} the maximum CO₂ absorption of the [C₂OHmim][Gly]/MDEA complex solution is 0.523 mol/mol, whereas the maximum absorption of [C₂OHmim][Lys]/MDEA is 0.75 mol/mol. What's more, the absorption rate and regeneration efficiency are also slightly higher than those of glycine-based ionic liquid. Therefore, compared with this system, it has been proven that the [C₂OHmim][Lys]/MDEA hybrid solution has better CO₂ absorption capacity and more potential as a green absorbent. Thus, the compound solution system in this work has a higher potential as a new industrial efficient absorbent.

This paper used a functionalized ionic liquid/amine complex aqueous solution to absorb CO₂ and investigated the flow and mass transfer performance in a microchannel. The mechanism between CO₂ and hybrid solution was analyzed. For the visualization study, a high-speed camera and the Image-Pro software were applied for recording gas–liquid flow regimes and processing the images, respectively. Furthermore, the influence of the two-phase flow ratio and ionic liquid

concentration on the gas content, specific surface area, bubble length, and mass transfer coefficient was studied, and correlations for predicting the volumetric mass transfer coefficient and initial bubble length were fitted.

2. EXPERIMENTS AND METHODOLOGY

2.1. Experiments. In this experiment, a mass flow meter (S4832, Beijing Sevenstar Flow Co., Ltd.) was used to adjust the gas phase flow rate and a syringe pump (Harvard 704500, Tianjin Yabao Technology Co., Ltd.) was used to deliver the liquid phase. Gas and liquid phases were injected separately from the branch and main channel into the microchannel. After mass transfer in the channel, the two-phase mixture flowed into a collector. A differential pressure sensor (3051TG1A2B, Beijing Far East Rosemont Instrument Co., Ltd.) was used for measuring the pressure at the gas inlet. Meanwhile, the channel outlet was connected to the atmosphere. A high-speed camera (AX100, Lingyun Technology Group Co., Ltd.) was connected to a computer for real-time observation and recording. The frame rate of the high-speed camera was set to 1500 fps. The recorded images were imported into the Image Pro Plus software for measurement after screening, and the length and width of each bubble were obtained. According to different operating conditions (such as gas–liquid flow rates, ionic liquid concentration), there are approximately 200–1500 images that need to be processed to obtain a single reported data point. And a light source was placed underneath the microchannel to make the image clearer. The experimental apparatus is shown in Figure 1.



Figure 1. Schematic diagram of the experimental apparatus.

Because polymers have high transparency and excellent mechanical properties, during this work, polymethylmethacrylate (PMMA) was used to fabricate a square microchannel with a 600 μm cross section. The gas and liquid inlets were 1 cm long, and the length of the main channel was 3 cm. During the experiment, CO_2 gas (Langfang Langwei Gas Factory) was used as the dispersed phase, and $[\text{C}_2\text{OHmim}][\text{Lys}]$ (Aladdin Chemical Reagent Co., Ltd.) + MDEA (Shanghai Macklin Biochemical Technology Co., Ltd.) + 0.3 wt % sodium dodecyl sulfate (SDS) (Shanghai Macklin Biochemical Technology Co., Ltd.) hybrid solvent was employed as the continuous phase. The SDS was added into a mixed aqueous solution at 0.3 wt % to reduce the surface tension of the solution and change the wettability of the microchannel wall so as to maintain the stability of the two-phase system. The concentration ratio of ionic liquid to amine was changed sequentially in the liquid phase, whereas total concentrations of

$[\text{C}_2\text{OHmim}][\text{Lys}]$ and MDEA were maintained at 1 mol/L. Figure 2 shows the molecular structures of $[\text{C}_2\text{OHmim}][\text{Lys}]$

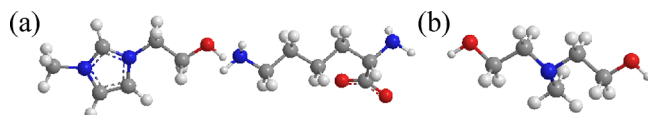


Figure 2. Molecular structure of (a) $[\text{C}_2\text{OHmim}][\text{Lys}]$ and (b) MDEA. (white: H; gray: C; blue: N; red: O).

and MDEA. In the experiment, the two-phase flow ratio ranged from 4 to 9, and the liquid flow rate was set as 20, 30, and 40 mL/h. Physical properties of blended solvents with different concentration ratios including surface tension (σ), viscosity (μ), and density (ρ) were measured by a surface tensiometer (DSA25S, Kruse Scientific Instruments Co., Ltd.) and a viscometer and densimeter (DMA5000, Austria Anton Paar Co., Ltd.), respectively. The measurement data are shown in Table 1.

Table 1. Physical Properties of the $[\text{C}_2\text{OHmim}][\text{Lys}]$ /MDEA Hybrid Solution

$C_{\text{IL}}/C_{\text{MDEA}}$	ρ (g/cm ³)	μ (mPa·s)	σ (mN/m)
0:10	1.008045	1.4059	36.63
1:9	1.012187	1.4729	35.61
2:8	1.016369	1.5870	34.49
3:7	1.020335	1.6384	33.92
4:6	1.024498	1.7292	32.37
5:5	1.028702	1.8285	31.96
6:4	1.032683	1.9255	31.59
7:3	1.036976	2.0469	31.02
8:2	1.041109	2.1699	30.85

2.2. Calculation Method. Figure 3 shows the schematic diagram of the bubble model. Under Taylor flow conditions,

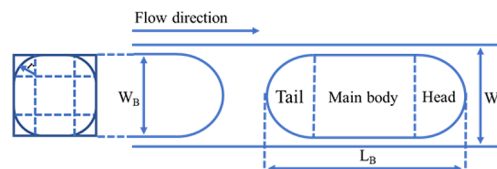


Figure 3. Schematic diagram of the bubble model.

the bubble consists of a main body (approximated to cylinder), a head, and a tail (approximated to hemispheres), and the cross-sectional area of the bubble body accounts for about 95% of the cross-sectional area of the channel. Hence, the area and volume of the Taylor bubbles in microchannels are calculated as follows:³⁶

$$A_B = \pi w_B^2 + [2\pi r + 4(w_B - 2r)](L_B - w_B) \quad (1)$$

$$V_B = 0.95w_B^2(L_B - w_B) + \frac{\pi w_B^3}{6} \quad (2)$$

$$r = w_B \sqrt{1/(40 - 10\pi)} \quad (3)$$

The formulas for calculating the surface area and volume of bubbly flow bubbles are as follows:

$$A_B = \pi L_B^2 \quad (4)$$

$$V_B = \frac{1}{6}\pi L_B^3 \quad (5)$$

where A_B is the surface area of the bubble (m^2), V_B is the volume of the bubble (m^3), w_B is the bubble width (m), L_B is the bubble length (m), and r is the fillet radius (m).

In addition, according to the relevant literature,^{34,35} the reaction of CO_2 and mixed solution can be assumed as a pseudo-first-order reaction. Although the microchannel reactor lacks stirring compared with the reactor in the literature, the liquid phase in the microchannel is far more excessive than the gas phase, and the residence time in the channel is very short, so the liquid phase is far from saturated after the reaction. More importantly, there are leakage flow and internal circulation in the liquid phase in the microchannel, which enhance the axial mixing and promote the material exchange between adjacent liquid slugs, which are beneficial to accelerate the surface renewal at the gas–liquid interface. Therefore, it can be assumed that the reaction of the system in the channel is a pseudo-first-order reaction, and mass transfer is the control step of the reaction rate. Because the gas phase was pure CO_2 , the mass transfer resistance of the gas film is negligible. Therefore, the volumetric mass transfer coefficient could be calculated as below:

$$k_L a = \frac{N_{\text{in}} - N_{\text{out}}}{\Delta C_m \cdot V_c} \quad (6)$$

where $k_L a$ is the liquid phase volumetric mass transfer coefficient (s^{-1}), k_L is the liquid phase mass transfer coefficient (m/s), N_{in} represents the gas molar flow rate at the inlet of the microchannel (mol/s), N_{out} represents the gas molar flow rate at the microchannel outlet (mol/s), ΔC_m represents the log-mean concentration (mol/m^3), and V_c represents the volume of the main channel (m^3).

The specific surface area could be calculated by:

$$a = \frac{\sum_{i=1}^m A_{Bi}}{V_c} \quad (7)$$

where m is the number of bubbles in the channel.

In addition, the total reaction rate could be expressed as below:

$$r_{\text{ov}} = (k_2 C_{\text{IL}} + k_2 C_{\text{MDEA}}) [\text{CO}_2] = k_{\text{ov}} [\text{CO}_2] \quad (8)$$

where k_{ov} is the overall rate constant (s^{-1}) and is expressed as $k_{\text{ov}} = k_{2,\text{IL}} C_{\text{IL}} + k_{2,\text{MDEA}} C_{\text{MDEA}}$ (the second-order rate constant $k_{2,\text{IL}}$, $k_{2,\text{MDEA}}$ ($\text{m}^3 \cdot \text{mol}^{-1} \cdot \text{s}^{-1}$) could be obtained from the literature^{37,38}).

Some literature summarized the effect of amino acid concentration on the reaction rate.³⁹ In this paper, the effect of ionic liquid concentration on the overall reaction rate constant (k_{ov}) was considered. The value of k_{ov} could directly reflect the speed of the chemical reaction rate, and the values of k_{ov} corresponding to different IL + MDEA concentrations are shown in Figure 4. The reaction rate constant increases with the $[\text{C}_2\text{OHmim}][\text{Lys}]$ concentration. In addition, the increase of $[\text{C}_2\text{OHmim}][\text{Lys}]$ concentration is beneficial to improve the enhancement factor. This indicates that the increase of ionic liquid concentration can significantly enhance the chemical action and improve the chemical absorption rate of CO_2 .

According to the data recorded by the differential pressure sensor, the total pressure difference between the inlet and

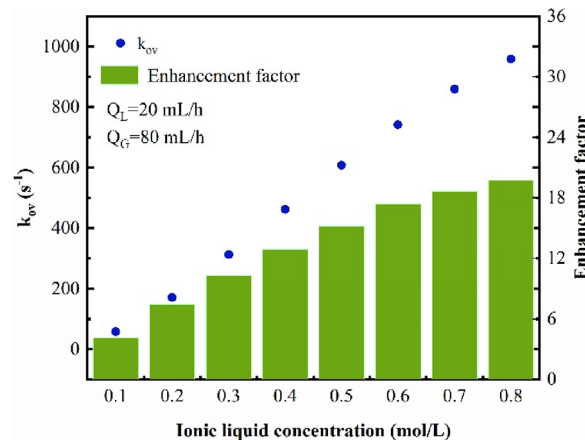


Figure 4. The overall reaction constant and enhancement factor of different $[\text{C}_2\text{OHmim}][\text{Lys}]$ concentrations at 298.15 K.

outlet is less than 7 kPa, so the bubbles' expansion and compression near the channel inlet and outlet of the channel could be ignored.⁴⁰ Thus, N_{in} and N_{out} could be obtained from the ideal gas equation of state:

$$N_{\text{in}} = \frac{p_{\text{in}} Q_G}{RT} \quad (9)$$

$$N_{\text{out}} = \frac{p_{\text{out}} V_{\text{CO}_2,\text{out}} f}{RT} \quad (10)$$

where the p_{in} is the pressure at the gas inlet (Pa), p_{out} is the atmosphere, Q_G is the volumetric flow rate of the gas phase (m^3/s), R is the ideal gas constant (J/mol/K), T is the temperature (K), $V_{\text{CO}_2,\text{out}}$ is the bubble volume at the channel outlet (m^3), and f is the bubble generation frequency (Hz).

Because of the excessive IL-amine mixed solution relative to CO_2 and fast reaction, the CO_2 concentration in the hybrid solvent is negligible. Therefore, the ΔC_m could be calculated by the CO_2 interfacial concentrations at the microchannel inlet and outlet.³³

$$\Delta C_m = \frac{C_{\text{in}}^* - C_{\text{out}}^*}{\ln(C_{\text{in}}^*/C_{\text{out}}^*)} \quad (11)$$

On the basis of Henry's law, the interfacial concentrations could be calculated as follows:

$$C_m^* = \frac{\bar{p}}{H} \quad (12)$$

where C_m^* represents the CO_2 interfacial concentration (mol/m^3), H represents Henry's constant ($\text{Pa}/(\text{mol}/\text{m}^3)$) that was calculated from the literature,³⁵ and \bar{p} is the average pressure (Pa).

The overall volumetric mass transfer coefficient could be obtained by eqs 6 and 9–12:

$$k_L a = \frac{N_{\text{in}} - N_{\text{out}}}{V_c \cdot \frac{(p_{\text{in}} - p_{\text{out}})}{H \cdot \ln(p_{\text{in}}/p_{\text{out}})}} = \frac{(N_{\text{in}} - N_{\text{out}}) \cdot H \cdot \ln(p_{\text{in}}/p_{\text{out}})}{V_c \cdot (p_{\text{in}} - p_{\text{out}})} \quad (13)$$

3. RESULT AND DISCUSSION

3.1. Flow Patterns. In the study, two flow regimes were observed as shown in Figure 5, including Taylor flow and a

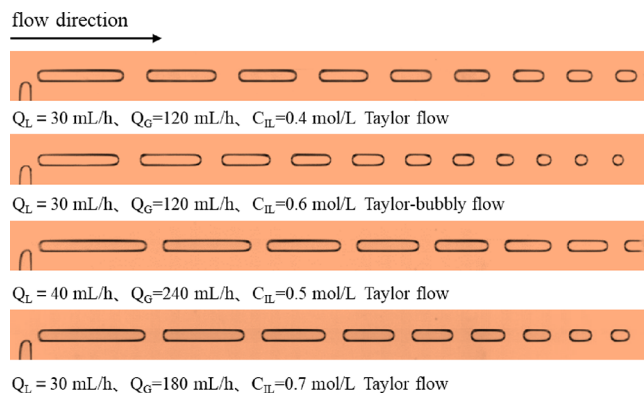


Figure 5. Flow regimes of two-phase flow in the microchannel.

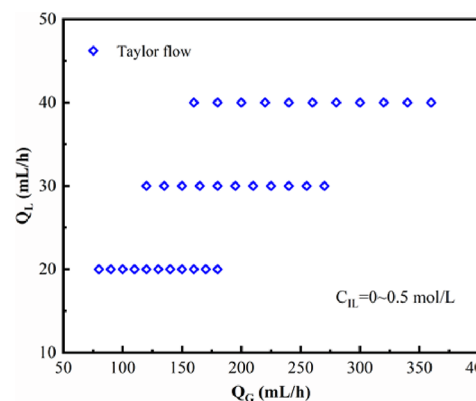
small amount of Taylor-bubbly flow. Taylor flow is of great interest to researchers because of its wide range of operating conditions. What's more, adjacent bubbles under Taylor flow are separated by liquid slugs, and there is no bubble coalescence, which make it easy to perform a visualization study. Therefore, the mass transfer process of CO_2 and $[\text{C}_2\text{OHmim}][\text{Lys}]$ /MDEA mixed aqueous solution was mainly studied under Taylor flow.

The flow pattern map is shown in Figure 6, in which the flow regime is mapped against the range of different gas and liquid flow rates investigated in this work. Under the gas and liquid flow rates studied in this experiment, all flow patterns are Taylor flow when the ionic liquid concentration is low ($C_{\text{IL}} = 0\text{--}0.5 \text{ mol/L}$). The absorption capacity of the liquid phase to CO_2 bubbles increased with the ionic liquid concentration, and the bubbles evolved into small spherical bubbles at the end of the channel ($C_{\text{IL}} = 0.6\text{--}0.8 \text{ mol/L}$). Meanwhile, the flow pattern transition line shifts to the right.

3.2. Stability Verification. Twenty bubbles at the T-junction were randomly selected as samples to analyze the length and velocity under $C_{\text{MDEA}} = 1.0 \text{ mol/L}$, $Q_{\text{L}} = 20 \text{ mL/h}$, and $Q_{\text{G}} = 80 \text{ mL/h}$. The relative standard variance was used as the criterion to evaluate the stability of the experiment, which could be calculated as follows:

$$S = \sqrt{\frac{1}{n} \sum_{i=1}^n (x_i - \bar{x})^2} \quad (14)$$

$$\text{RSD} = \frac{S}{\bar{x}} \times 100\% \quad (15)$$



where S is the standard variance, n is the number of sample bubbles, \bar{x} is the statistical mean, and RSD is the relative standard variance.

Figure 7 shows the stability of bubble velocity and length. As described in Figure 7, the relative standard variances are both

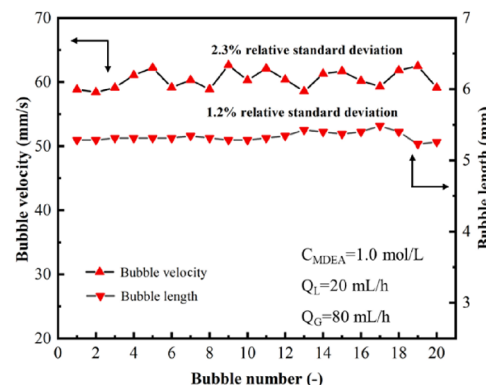


Figure 7. Stability verification of bubble velocity and length.

less than 5%, which indicate that the bubbles generated by this experiment are reproducible and can be further studied. During the experiment, the specific reasons for fluctuations in bubble length and velocity are divided into two aspects. First, the mass transfer of two phases at the T-junction leads to pressure fluctuation. Second, the working principle of the syringe pump has an impact on the pressure.

3.3. Evolution of Bubble Length and Liquid Film Thickness in the Microchannel. The evolution of bubbles along the channel was recorded by a high-speed camera. Subsequently, by using the Image Pro Plus software to process the flow pattern images, the bubble length at different positions of the channel was quantified. The influence of $[\text{C}_2\text{OHmim}][\text{Lys}]$ concentration and gas flow rates on bubble length is displayed in Figure 8, where X indicates the distance between the T-junction and the center of bubbles. The bubble center coordinates were tracked to obtain the variation of bubble length at different positions in the microchannel.

Under the combined action of inertia force, shear force, and pressure drop, the constraint of surface tension is overcome, and then bubbles are gradually formed in the T-junction. The bubble length is significantly shortened in the beginning stage of bubble formation; this is due to the strong mass transfer driving force between CO_2 and $[\text{C}_2\text{OHmim}][\text{Lys}]$ /MDEA

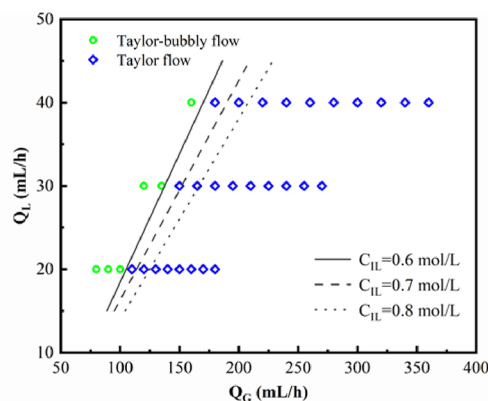


Figure 6. Flow regime maps of different operating conditions.

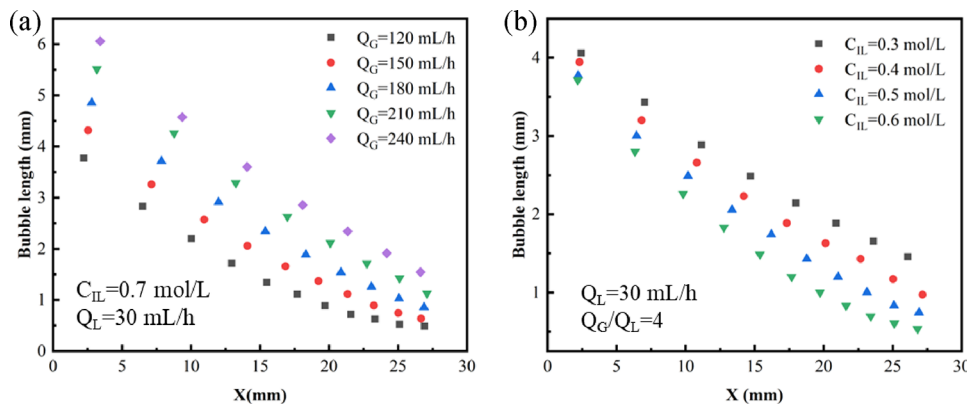


Figure 8. Influence of (a) gas flow rates and (b) $[C_2OHmim][Lys]$ concentration on bubble length.

hybrid solution, which makes the gas be absorbed quickly. With bubble flowing along the channel, the CO_2 concentration absorbed into the hybrid solution increases, so the solute concentration decreases relatively, resulting in the decline of the mass transfer driving force as well as the weakening of the chemical reaction between two phases. Thus, the CO_2 absorption rate would slow down, resulting in a gradual decrease in bubble shrinkage as the bubble moves forward along the channel. The effects of gas flow rates on bubble length along the channel is shown in Figure 8a; at a given $[C_2OHmim][Lys]$ concentration and liquid flow rate, the higher the gas flow rate is, the longer is the initial bubble length. Meanwhile, with the increase of gas flow rate, the update rate at the two-phase interface would be accelerated; another key fact to remember is that the disturbance inside the liquid slug would become more intense. These all contribute to the CO_2 absorption process. Therefore, the bubble length total reduction increases with the gas flow rates. The variation of bubble length with $[C_2OHmim][Lys]$ concentration is shown in Figure 8b. When two-phase flow rates are fixed, increasing the $[C_2OHmim][Lys]$ concentration would accelerate the chemical reaction rate, resulting in bubbles being rapidly absorbed by the surrounding liquid phase. The reduction of the initial bubble length and the rapid shortening of the bubble length are reflected in the experimental data.

A significant feature of Taylor flow is the existence of a liquid film between the dispersed liquid slug and the channel wall. The thickness of the liquid film has a great influence on the mass and heat transfer rate. Under the Taylor flow pattern of gas–liquid two-phase flow in the channel, the researchers studied the liquid film and proposed some models to predict the liquid film thickness. The results show that in the square channel, the liquid film thickness is almost a certain value when the capillary number Ca is less than 0.02,⁴¹ so we select the liquid film thickness at the center of each bubble as the representative of the bubble. Because the liquid film thickness is relatively small, the direct measurement error is large through the Image Pro Plus software. To minimize the error, we calculate the liquid film thickness by measuring the width of each bubble and using the difference between the channel width and the bubble width. The variation of liquid film thickness along the channel length is shown in Figure 9. With the mass transfer process, the liquid film thickness showed an increasing trend, but the overall growth was not large. Because the mass transfer between the bubble caps and the adjacent liquid slug is relatively strong, on the contrary, the mass

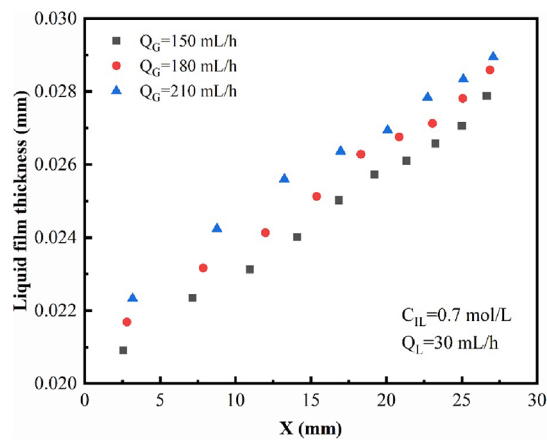


Figure 9. The variation of liquid film thickness along the microchannel.

transfer between the bubble main body and the liquid film near the channel wall is relatively weak. Therefore, it can be observed during the experiment that the length of the Taylor bubble decreases significantly with the mass transfer, whereas the bubble width does not change much. Therefore, the thickness of the liquid film gradually increases along the channel length, but the overall change is less. In addition, the increase of gas flow rate is beneficial to the increase of liquid film thickness because the bubble velocity increases with the increase of gas flow rate, which is beneficial to the increase of capillary number.

The length of a new generated bubble that has regular head and tail at the T-junction is regarded as the initial bubble length ($L_{B,0}$). The ratio of $L_{B,0}$ to the width of the microchannel (w) is defined as the dimensionless initial bubble length ($L_{B,0}/w$). Figure 10 shows the effect of the two-phase flow ratio (Q_G/Q_L) on the dimensionless initial bubble length. It could be clearly found from Figure 10 that the initial bubble length increases with Q_G/Q_L . When the liquid capillary number is less than 0.01, the bubble formation process conforms to the squeezing mechanism. Studies have shown a linear relationship between $L_{B,0}/w$ and Q_G/Q_L under this condition as below:⁴²

$$\frac{L_{B,0}}{w} = \alpha + \beta \frac{Q_G}{Q_L} \quad (16)$$

where $L_{B,0}$ is the initial bubble length (m) and w is the width of the microchannel (m).

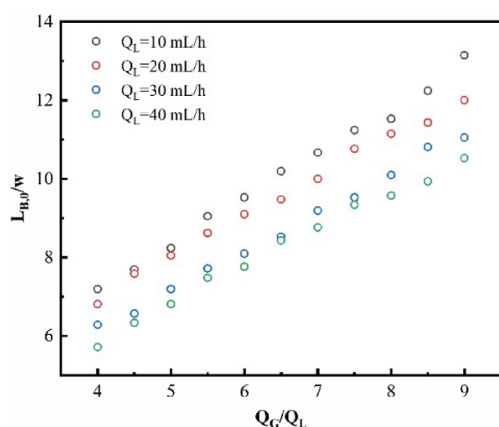


Figure 10. Influence of two-phase flow ratio on L_0/w ($C_{IL} = 0.7 \text{ mol/L}$).

By substituting the data into Matlab for fitting, the variables in eq 16 could be solved: $\alpha = 0.613$ and $\beta = 1.4886$. The alpha and beta values under other ionic liquid concentrations are shown in Table 2. Figure 11 shows the comparison between

Table 2. The Alpha and Beta Values under Different Ionic Liquid Concentrations

C_{IL}/C_{MDEA}	alpha	beta
0:10	3.7698	0.9935
1:9	4.0434	0.9218
2:8	2.8677	1.0579
3:7	2.7311	1.0414
4:6	3.2506	0.9499
5:5	2.8833	0.9944
6:4	2.2055	1.0154
8:2	2.5856	0.9645

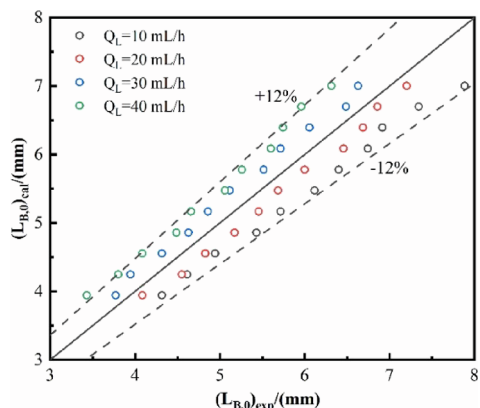
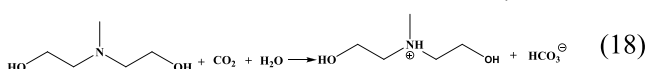
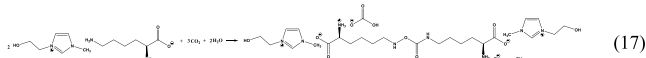


Figure 11. Comparison between experimental data and predicted values for initial bubble length ($C_{IL} = 0.7 \text{ mol/L}$).

experimental data and predicted values by eq 14 for the initial bubble length, and the relative deviation is within 12%, indicating a good prediction performance.

3.4. Gas–Liquid Reaction Mechanism Analysis.



The reaction mechanism between CO_2 and the $[\text{C}_2\text{OHmim}][\text{Lys}]$ /MDEA blended solvent is indicated in Figure 12. A relatively simple version of the reaction mechanism flowchart can be found in the Supporting Information. The ionic liquid $[\text{C}_2\text{OHmim}][\text{Lys}]$ was dissociated into cation ($[\text{C}_2\text{OHmim}]^+$) and anion ($[\text{Lys}]^-$) in water by solvation. The anion ($[\text{Lys}]^-$) became the major reactive species due to its stronger alkalinity than MDEA. The reaction of lysine with CO_2 could be divided into two steps:³⁷ First, carbamate is produced via the reaction between $[\text{Lys}]^-$ and CO_2 , and then the carbamate near the carboxylic acid of lysine is hydrolyzed. Subsequently, the generated products play a catalytic role in promoting the hydration reaction of MDEA to generate MDEAH^+ and HCO_3^- . In addition, the cation ($[\text{C}_2\text{OHmim}]^+$) would probably not participate in the reaction.

3.5. Specific Surface Area and Gas Holdup. The gas holdup is an important parameter to evaluate the performance of a reactor, which is defined as the volume fraction of the gas phase in a multiphase flow system. At the same time, the gas holdup in the microchannel is necessary for predicting mass and heat transfer efficiency and flow pattern transition. In general, the gas and liquid phases' contact area increases with gas content, which is favorable to reduce energy consumption and enhance the two-phase mass transfer. The gas holdup (ε) could be estimated from eq. 19:

$$\varepsilon = \frac{\sum_{i=1}^m V_{Bi}}{V_c} \quad (19)$$

where m is the number of bubbles in the channel.

Because the volume of the microchannel is fixed, the gas holdup and specific surface area showed similar trends under the same experimental conditions. Figure 13a shows the effects of the two-phase flow ratio (Q_G/Q_L) on the specific surface area and gas holdup. For a given $[\text{C}_2\text{OHmim}][\text{Lys}]$ concentration, the increase of Q_G/Q_L could generate a remarkable increase in the specific surface area and gas holdup because the bubbles are elongated and liquid slugs are shortened. The flow pattern would develop to transition flow during the two-phase flow ratio increases to a certain extent, and then the increase of Q_G/Q_L has no significant effect on the specific surface area as well as gas holdup. Therefore, the increasing trend of specific surface area and gas holdup gradually slows down. The effects of $[\text{C}_2\text{OHmim}][\text{Lys}]$ concentration on the specific surface area and gas holdup are depicted in Figure 13b. When Q_G/Q_L is fixed, larger specific surface area and gas holdup are obtained under lower $[\text{C}_2\text{OHmim}][\text{Lys}]$ concentrations. As shown in Table 1, the surface tension of the mixed solution decreases with the elevated $[\text{C}_2\text{OHmim}][\text{Lys}]$ concentration, causing the decrease of initial bubble length, which thereby causes smaller specific surface area and gas holdup. Furthermore, for a given Q_G/Q_L , the chemical reaction between the gas and liquid phase is enhanced with the increase of $[\text{C}_2\text{OHmim}][\text{Lys}]$ concentration, leading to the increase of CO_2 absorption rate. Consequently, the bubble length in channel would shorten so that the specific surface area and gas holdup decrease.

The total residence time (t_r) is defined as the time from the generation of a single bubble at the T-junction to leaving the channel. The variation of gas holdup with total residence time is shown in Figure 14. For a given liquid flow rate, the gas holdup increases and the total residence time decreases with

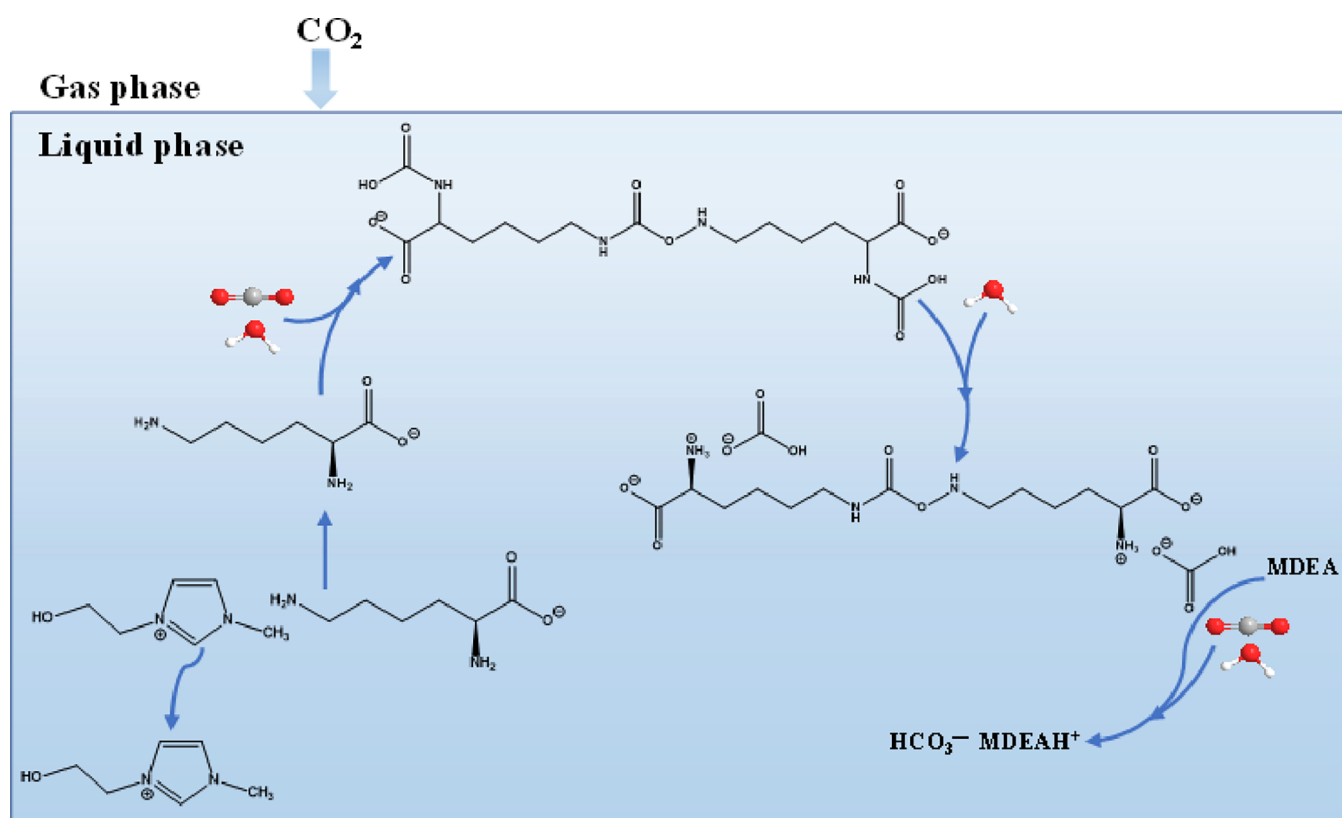


Figure 12. Reaction mechanism of CO_2 with $[\text{C}_2\text{OHmim}][\text{Lys}]$ /MDEA.

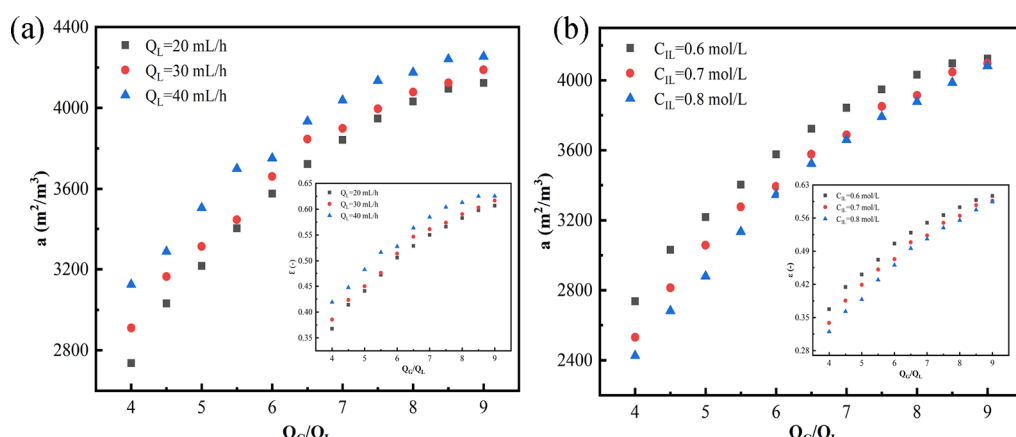


Figure 13. Effects of (a) gas–liquid two-phase flow ratio ($C_{\text{IL}} = 0.6 \text{ mol/L}$) and (b) $[\text{C}_2\text{OHmim}][\text{Lys}]$ concentration ($Q_L = 20 \text{ mL/h}$) on specific surface area and gas holdup.

the Q_G/Q_L . This is because the increase of Q_G/Q_L is beneficial to elongate bubble length and accelerate bubble velocity. At the same ionic liquid concentration, the absorption capacity of the liquid phase to bubbles is uniform under different operating conditions. Therefore, at high gas flow rates, the bubble velocity increases, which shortens the contact time between the bubble and the liquid slug and weakens the effect of bubble residence time growth due to gas dissolution in the liquid phase.

3.6. Effects of Two-Phase Flow Rates on Mass Transfer. Figure 15a shows the effects of the two-phase flow ratio (Q_G/Q_L) on the liquid phase mass transfer coefficient (k_L). The results show that k_L is elevated slightly by increasing the two-phase flow ratio, and k_L is more affected by liquid

phase flow rates. For a fixed liquid phase flow rate, increasing Q_G/Q_L could accelerate the internal circulation rate inside the liquid slug, thus enhancing the mass transfer process.⁴³ For a given Q_G/Q_L , larger liquid flow rates would cause higher gas flow rates, increasing the degree of disturbance to liquid slug. In addition, the increase of Q_G/Q_L could accelerate the movement rate of the bubbles, which would reduce the residence time of the bubbles in the straight channel. On the basis of the solute permeation theory, for the gas–liquid two-phase mass transfer process, the fluid at the phase interface is always continuously mixed with the liquid phase to expose a new contact surface. The solute continuously penetrates from the phase interface to the main body of the liquid phase through molecular diffusion, and there are different instanta-

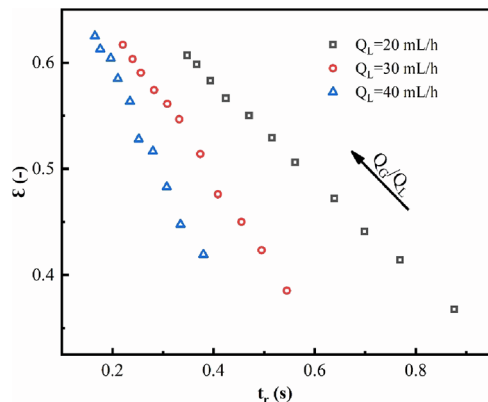


Figure 14. The variation of gas holdup with total residence time ($C_{IL} = 0.6 \text{ mol/L}$).

neous concentration distributions and corresponding instantaneous diffusion rates (proportional to the concentration gradient at the phase interface) at each moment. The longer the exposure time of the fluid surface is, the smoother the concentration distribution curve in the liquid film is, and the lower the solute diffusion rate at the interface is. Therefore, because of the increase of Q_G/Q_L , the gas–liquid contact time is shortened and the concentration distribution curve becomes steeper, which is beneficial to the diffusion process of CO_2 at the phase interface, thereby improving the mass transfer performance.⁴⁴ Moreover, at a fixed liquid flow rate, increasing the Q_G/Q_L could increase the bubble length and shorten the liquid slug length between the two bubbles, which would reduce the mass transfer efficiency between the bubble and the liquid slug. Therefore, the variation of k_L with Q_G/Q_L is the result of the above factors.

Figure 15b indicates the influence of the Q_G/Q_L on the liquid phase volumetric mass transfer coefficient ($k_{L,a}$). It illustrates that the increase of Q_G/Q_L could significantly improve $k_{L,a}$. At the same Q_G/Q_L , comparatively, the lower the liquid flow rate is, the flatter is the growth trend of $k_{L,a}$. When the liquid phase flow rate is fixed, increasing Q_G/Q_L could considerably increase the specific surface area because of the increase of bubble length so as to improve mass transfer performance. What's more, compared with the contribution of Q_G/Q_L to k_L , the increase of specific surface area is the key factor for $k_{L,a}$ to increase with Q_G/Q_L . At large Q_G/Q_L , the flow pattern develops to transition flow, and the increase rate of the

specific surface area slows down and gradually approaches an almost constant value. Therefore, $k_{L,a}$ will increase quickly at first and then tend to be stable as described in the literature.⁴⁵ For a given Q_G/Q_L , the gas flow rates increase with the liquid phase flow rates, and the squeezing effect of bubbles on liquid plug would be enhanced, which could intensify the internal circulation in the liquid plug, thus increasing $k_{L,a}$.

3.7. Effects of $[\text{C}_2\text{OHmim}][\text{Lys}]$ Concentration on Mass Transfer. Figure 16 illustrates the variation of the k_L and $k_{L,a}$ against ionic liquid concentration. It could be observed from Figure 16 that k_L and $k_{L,a}$ increase significantly when adding ionic liquid into MDEA aqueous solution. For a fixed two-phase flow rate, the higher the ionic liquid ($[\text{C}_2\text{OHmim}][\text{Lys}]$) concentration is, the larger both k_L and $k_{L,a}$ are. Upon increasing the $[\text{C}_2\text{OHmim}][\text{Lys}]$ concentration, the chemical reaction could be enhanced, which would accelerate the CO_2 absorption rate by the liquid phase, causing the CO_2 concentration gradient at the two-phase interface to increase. What's more, the liquid phase mass transfer resistance decreases. Moreover, the addition of $[\text{C}_2\text{OHmim}][\text{Lys}]$ could effectively increase the total reaction rate constant (as shown in Figure 4) so that the reaction rate of the mixed solution with CO_2 is accelerated. Consequently, as shown in Figure 16a, k_L would be improved with increasing $[\text{C}_2\text{OHmim}][\text{Lys}]$ concentration. The variation trend of liquid phase volumetric mass transfer coefficient ($k_{L,a}$) is originated in the combined contribution of specific surface area (a) and liquid phase mass transfer coefficient (k_L). The chemical reaction rate increases with the $[\text{C}_2\text{OHmim}][\text{Lys}]$ concentration, so the absorption of bubbles by the liquid phase is accelerated, resulting in the decrease of bubble volume and the increase of the number of bubbles in the channel, which increases the contact area between the head and tail of bubbles and the liquid slug, which is conducive to improving mass transfer. At the same time, because of the rapid chemical reaction, the bubble length is shortened and the specific surface area is decreased, which is not beneficial to the improvement of $k_{L,a}$. As shown in Figure 16b, $k_{L,a}$ increases with the $[\text{C}_2\text{OHmim}][\text{Lys}]$ concentration because the enhancement effect of ionic liquid on k_L is significantly stronger than the weakening effect of specific surface area (a). Furthermore, with the rising of $[\text{C}_2\text{OHmim}][\text{Lys}]$ concentration, the viscosity of mixed solution increases, and then the bubble velocity decreases because of the rapid chemical absorption. Moreover, as the bubble is continuously absorbed by the liquid phase, the viscosity of the liquid slug will gradually increase, which also

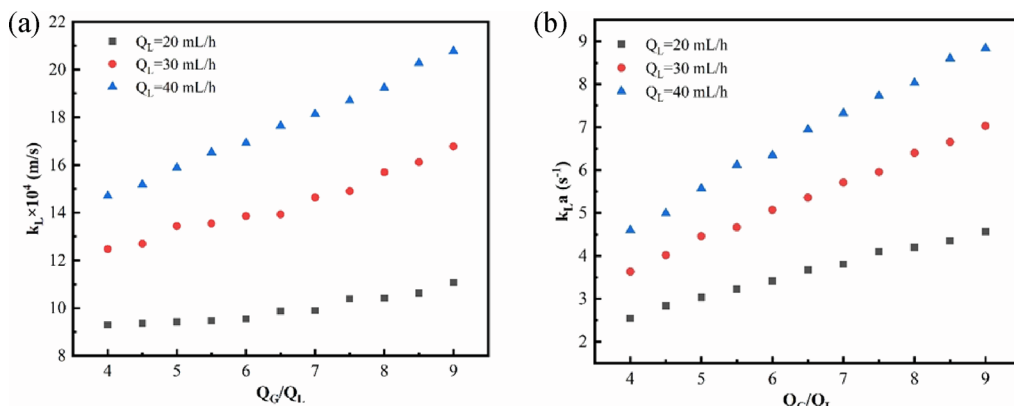


Figure 15. Effects of two-phase flow ratio on the (a) mass transfer coefficient and (b) volumetric mass transfer coefficient ($C_{IL} = 0.6 \text{ mol/L}$).

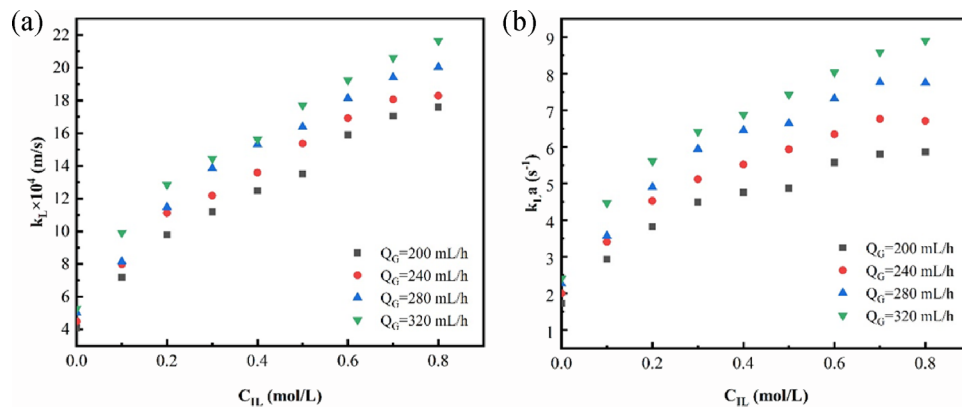


Figure 16. Effects of ionic liquid concentration on the (a) mass transfer coefficient and (b) volumetric mass transfer coefficient ($Q_L = 40$ mL/h).

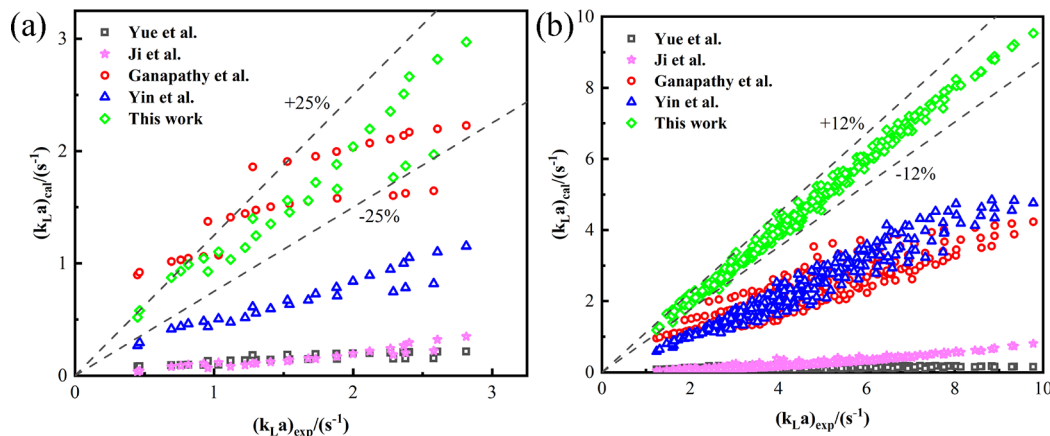


Figure 17. Comparison of $k_{L,a}$ in (a) 1 mol/L MDEA and (b) mixed aqueous solution of IL/MDEA between experimental results and calculated values.

affects the velocity of the liquid slug and the bubble in the channel so that the bubble residence time in the microchannel is prolonged. As the bubble moves along the channel, the concentration of the absorbent in the liquid phase gradually decreases, which will lead to a decrease in the mass transfer enhancement of the chemical reaction, so the dynamic mass transfer coefficient along the channel direction will become smaller and smaller. In addition, it is proven that the average liquid mass transfer coefficient is negatively correlated with the total residence time of bubbles.⁴⁶ Therefore, the prolongation of residence time weakens the mass transfer performance and is unfavorable to increase $k_{L,a}$. Therefore, the variation of $k_{L,a}$ against the concentration of $[C_2OHmim][Lys]$ is affected by the comprehensive competition of the above multiple factors.

3.8. Prediction of Mass Transfer Coefficient. So far, many researchers have focused on the establishment of a liquid mass transfer coefficient prediction model. In previous studies, some correlations for predicting the $k_{L,a}$ of CO_2 absorbed into different systems in microchannels with various configurations have been proposed. Yue et al.⁴⁷ explored the physical absorption performance of CO_2 into water in a microchannel, and a dimensionless correlation was proposed to predict $k_{L,a}$:

$$Sh_L ad_h = 0.084 Re_G^{0.213} Re_L^{0.937} Sc_L^{0.5} \quad (20)$$

where Sh_L is the liquid phase Sherwood number that is defined as $Sh_L = k_L d_h / D$. d_h is the hydraulic diameter of the channel (m). Re_G and Re_L are the gas and liquid phase Reynolds number, respectively, which could be defined as $Re_G = d_h u_G \rho_G / \mu_G$

and $Re_L = d_h u_L \rho_L / \mu_L$. Sc_L is the liquid phase Schmidt number that could be expressed as $Sc_L = \mu_L / D \rho_L$. ρ and μ are the density (kg/m³) and viscosity (Pa·s), respectively. u is the velocity (m/s). D is the diffusion coefficient of CO_2 in the liquid phase (m²/s), which can be calculated from the literature.⁴⁸

Furthermore, Ji et al.⁴⁹ designed three different dimensions of the microchannels and studied the mass transfer characteristics of CO_2 –water, CO_2 –ethanol, and CO_2 –*n*-propanol in microchannels with different hydraulic diameters. A new correlation containing the capillary number for predicting $k_{L,a}$ was proposed:

$$Sh_L ad_h = 0.22 Re_G^{0.78} Re_L^{0.0535} Sc_L Ca_L^{0.7586} \quad (21)$$

In addition, Ganapathy et al.⁵⁰ studied the chemical absorption of CO_2 by diethanolamine in microchannels with different hydraulic diameters and established a prediction formula of $k_{L,a}$:

$$Sh_L = 1.689 \times 10^{-4} Re_G^{0.223} Re_L^{0.829} Sc_L^{1.766} \quad (22)$$

Moreover, Yin et al.⁴⁶ studied the absorption process of CO_2 into $[\text{Bmim}][\text{BF}_4]/\text{monoethanolamine}$ hybrid solvent in a T-shaped microchannel. They adopted the Damköhler number (which is expressed as $Da = k_{ov} d_h^2 / D$) to characterize the influence of chemical reaction, and an empirical correlation of $k_{L,a}$ was obtained:

$$Sh_L ad_h = 0.81 Re_G^{0.78} Re_L^{0.41} Da^{0.35} \quad (23)$$

The comparison of k_{La} between experimental data and calculated results by the above empirical correlations is shown in Figure 17. It could be clearly found that the predicting values have obvious deviations from the experiment. The enhancement of chemical reaction between CO_2 and functional ionic liquid $[\text{C}_2\text{OHmim}][\text{Lys}]$ on mass transfer was considered. The enhancement factor was introduced into the ionic liquid system, which is defined as follows:

$$E = \sqrt{k_{ov} D_{\text{CO}_2}} / k_p \quad (24)$$

k_p is the liquid-side physical mass transfer coefficient (m/s), which could be calculated based on the permeation theory:

$$k_p = 2\sqrt{D_{\text{water}}/\pi t_c} \quad (25)$$

where D_{water} is the diffusion coefficient of CO_2 in water (m^2/s). t_c is the time of mass transfer (s).

Therefore, two modified dimensionless correlations for predicting k_{La} were proposed by fitting experimental data.

For the MDEA aqueous solution:

$$Sh_{La}d_h = 2.7184 Re_G^{0.9283} Re_L^{0.5015} Sc_L^{0.2314} \quad (26)$$

For the $[\text{C}_2\text{OHmim}][\text{Lys}]$ -MDEA hybrid aqueous solution:

$$Sh_{La}d_h = 0.3639 Re_G^{1.0604} Re_L^{0.1588} Sc_L^{0.6045} E^{0.4880} \quad (27)$$

The comparison between experimental results and calculated values by eqs 26 and 27 is shown in Figure 17, and the relative deviations are within $\pm 25\%$ and $\pm 12\%$, which show a good prediction performance. As shown in Figure 17, the k_{La} in the MDEA aqueous solution ranges from 0.5 to 3; however, the k_{La} in the $[\text{C}_2\text{OHmim}][\text{Lys}]$ /MDEA hybrid aqueous solution ranges from 1 to 10. The reason for the difference is that the anions in the ionic liquid have stronger alkalinity than MDEA and could react rapidly with CO_2 , which could effectively improve k_{La} . In addition, because Figure 17a only includes data under one concentration condition, the fitting error is larger than that of the hybrid solution.

4. CONCLUSIONS

In the experiment, the flow and mass transfer characteristics of CO_2 chemical absorption in the hybrid solvent of a functional ionic liquid ($[\text{C}_2\text{OHmim}][\text{Lys}]$) and *N*-methyldiethanolamine (MDEA) were investigated in a T-shaped microchannel by the visualization analysis method. The stability of the experiment was analyzed to ensure good reproducibility of the data. Taylor-bubbly flow and Taylor flow were recorded during this experiment, and the variation of bubble length along the channel was also observed. It could be found that increasing the gas flow rates could effectively lengthen the initial bubble length, whereas increasing the $[\text{C}_2\text{OHmim}][\text{Lys}]$ concentration results in the opposite. Meanwhile, the influence of Q_G/Q_L on dimensionless initial bubble length was investigated, and a new linear correlation for predicting initial bubble length was established. The effects of Q_G/Q_L and $[\text{C}_2\text{OHmim}][\text{Lys}]$ concentration on gas holdup, specific surface area, k_L , and k_{La} were investigated experimentally. The results show that gas holdup and specific surface area have similar variation trend; both increase with Q_G/Q_L and gradually stabilize. However, the increase of $[\text{C}_2\text{OHmim}][\text{Lys}]$ concentration would reduce the specific surface area and gas holdup. Besides, the increase of Q_G/Q_L can enhance the disturbance to the liquid slug, which would increase k_L and k_{La} . Comparatively, the mass transfer

performance is more affected by liquid flow rates. Also, increasing the $[\text{C}_2\text{OHmim}][\text{Lys}]$ concentration would accelerate the reaction rate and enhance mass transfer. Hence, in the aqueous solution system, the addition of $[\text{C}_2\text{OHmim}][\text{Lys}]$ to MDEA could effectively improve the mass transfer performance. The enhancement factor E representing the enhancement of the chemical reaction on mass transfer was introduced in the system containing ionic liquid. Two new correlations were proposed to predict k_{La} , which have satisfactory predicting performance.

ASSOCIATED CONTENT

Supporting Information

The Supporting Information is available free of charge at <https://pubs.acs.org/doi/10.1021/acs.iecr.2c04407>.

A simple flowchart of the reaction mechanism between $[\text{C}_2\text{OHmim}][\text{Lys}]$ /MDEA aqueous solution and CO_2 (PDF)

AUTHOR INFORMATION

Corresponding Authors

Haifeng Dong – Beijing Key Laboratory of Ionic Liquids Clean Process, State Key Laboratory of Multiphase Complex Systems, Institute of Process Engineering, Chinese Academy of Science, Beijing 100190, China; Advanced Energy Science and Technology Guangdong Laboratory, Huizhou 516227 Guangdong, China;  orcid.org/0000-0002-9821-1572; Email: hfdong@ipe.ac.cn

Changyu Sun – State Key Laboratory of Heavy Oil Processing, China University of Petroleum, Beijing 102249, China;  orcid.org/0000-0001-6931-6554; Email: cysun@cup.edu.cn

Authors

Zhenbin Xu – State Key Laboratory of Heavy Oil Processing, China University of Petroleum, Beijing 102249, China; Beijing Key Laboratory of Ionic Liquids Clean Process, State Key Laboratory of Multiphase Complex Systems, Institute of Process Engineering, Chinese Academy of Science, Beijing 100190, China; Advanced Energy Science and Technology Guangdong Laboratory, Huizhou 516227 Guangdong, China

Tingting Wang – Beijing Key Laboratory of Ionic Liquids Clean Process, State Key Laboratory of Multiphase Complex Systems, Institute of Process Engineering, Chinese Academy of Science, Beijing 100190, China; Advanced Energy Science and Technology Guangdong Laboratory, Huizhou 516227 Guangdong, China

Jianmeng Wu – Beijing Key Laboratory of Ionic Liquids Clean Process, State Key Laboratory of Multiphase Complex Systems, Institute of Process Engineering, Chinese Academy of Science, Beijing 100190, China; Advanced Energy Science and Technology Guangdong Laboratory, Huizhou 516227 Guangdong, China;  orcid.org/0000-0002-9992-3897

Lulu Wang – Beijing Key Laboratory of Ionic Liquids Clean Process, State Key Laboratory of Multiphase Complex Systems, Institute of Process Engineering, Chinese Academy of Science, Beijing 100190, China; Advanced Energy Science and Technology Guangdong Laboratory, Huizhou 516227 Guangdong, China

Xiangping Zhang – Beijing Key Laboratory of Ionic Liquids Clean Process, State Key Laboratory of Multiphase Complex

Systems, Institute of Process Engineering, Chinese Academy of Science, Beijing 100190, China; Advanced Energy Science and Technology Guangdong Laboratory, Huizhou 516227 Guangdong, China;  orcid.org/0000-0002-1431-0873

Complete contact information is available at:

<https://pubs.acs.org/10.1021/acs.iecr.2c04407>

Notes

The authors declare no competing financial interest.

ACKNOWLEDGMENTS

This work is financially supported by the National Key Research and Development Program of China (2020YFA0710204) and 2021 Industrial Technology Basic Public Service Platform Project-Public Service Platform for Emission Peak and Carbon Neutral of Key Raw Material Industries (2021-H029-1-1). We sincerely appreciate Prof. Suojiang Zhang (IPE, CAS) for his careful academic guidance and great support.

REFERENCES

- (1) Murai, S.; Fujioka, Y. Challenges to the carbon dioxide capture and storage (CCS) technology. *IEEJ Trans. Electr. Electron. Eng.* **2008**, *3*, 37–42.
- (2) Xie, W.-H.; Li, H.; Yang, M.; He, L.-N.; Li, H.-R. CO₂ capture and utilization with solid waste. *Green Chem. Eng.* **2022**, *3*, 199–209.
- (3) Knuutila, H. K.; Rennemo, R.; Ciftja, A. F. New solvent blends for post-combustion CO₂ capture. *Green Energy Environ.* **2019**, *4*, 439–452.
- (4) Ramezani, R.; Di Felice, R. Kinetics study of CO₂ absorption in potassium carbonate solution promoted by diethylenetriamine. *Green Energy Environ.* **2021**, *6*, 83–90.
- (5) Siani, G.; Tiecco, M.; Di Profio, P.; Guernelli, S.; Fontana, A.; Ciulla, M.; Canale, V. Physical absorption of CO₂ in betaine/carboxylic acid-based Natural Deep Eutectic Solvents. *J. Mol. Liq.* **2020**, *315*, No. 113708.
- (6) Zhang, Z.; Chen, F.; Rezakazemi, M.; Zhang, W.; Lu, C.; Chang, H.; Quan, X. Modeling of a CO₂-piperazine-membrane absorption system. *Chem. Eng. Res. Des.* **2018**, *131*, 375–384.
- (7) Lilleby Helberg, R. M.; Dai, Z.; Ansaloni, L.; Deng, L. PVA/PVP blend polymer matrix for hosting carriers in facilitated transport membranes: Synergistic enhancement of CO₂ separation performance. *Green Energy Environ.* **2020**, *5*, 59–68.
- (8) Gao, Z.; Wang, Y.; Wu, H.; Ren, Y.; Guo, Z.; Liang, X.; Wu, Y.; Liu, Y.; Jiang, Z. Surface functionalization of Polymers of Intrinsic Microporosity (PIMs) membrane by polyphenol for efficient CO₂ separation. *Green Chem. Eng.* **2021**, *2*, 70–76.
- (9) Helberg, R. M. L.; Torstensen, J. Ø.; Dai, Z.; Janakiram, S.; Chinga-Carrasco, G.; Gregersen, Ø. W.; Syverud, K.; Deng, L. Nanocomposite membranes with high-charge and size-screened phosphorylated nanocellulose fibrils for CO₂ separation. *Green Energy Environ.* **2021**, *6*, 585–596.
- (10) Yin, J.; Gao, J.; Tong, M.; Chen, X.; Kang, W.; Zhou, Y.; Lu, J. Absorption and regeneration characteristics of alkanolamines after CO₂ removal from flue gas. *Energy Sources, Part A* **2016**, *38*, 3202–3206.
- (11) Mohammadi Noureddinvand, V.; Heidari, A. Experimental study of CO₂ absorption with MEA solution in a novel Arc-RPB. *Chem. Eng. Process.* **2021**, *165*, No. 108450.
- (12) Hemmati, A.; Rashidi, H.; Behradfar, K.; Kazemi, A. A comparative study of different mass transfer and liquid hold-up correlations in modeling CO₂ absorption with MEA. *J. Nat. Gas Sci. Eng.* **2019**, *62*, 92–100.
- (13) Ferrara, G.; Lanzini, A.; Leone, P.; Ho, M. T.; Wiley, D. E. Exergetic and exergoeconomic analysis of post-combustion CO₂ capture using MEA-solvent chemical absorption. *Energy* **2017**, *130*, 113–128.
- (14) Liu, Y.; Fan, W.; Wang, K.; Wang, J. Studies of CO₂ absorption/regeneration performances of novel aqueous monoethanolamine (MEA)-based solutions. *J. Cleaner Prod.* **2016**, *112*, 4012–4021.
- (15) Choi, W.-J.; Seo, J.-B.; Jang, S.-Y.; Jung, J.-H.; Oh, K.-J. Removal characteristics of CO₂ using aqueous MEA/AMP solutions in the absorption and regeneration process. *J. Environ. Sci.* **2009**, *21*, 907–913.
- (16) Veawab, A.; Tontiwachwuthikul, P.; Chakma, A. Corrosion behavior of carbon steel in the CO₂ absorption process using aqueous amine solutions. *Ind. Eng. Chem. Res.* **1999**, *38*, 3917–3924.
- (17) Zhang, Y.; Ji, X.; Xie, Y.; Lu, X. Screening of conventional ionic liquids for carbon dioxide capture and separation. *Appl. Energy* **2016**, *162*, 1160–1170.
- (18) Simon, N. M.; Zanatta, M.; dos Santos, F. P.; Corvo, M. C.; Cabrita, E. J.; Dupont, J. Carbon Dioxide Capture by Aqueous Ionic Liquid Solutions. *ChemSusChem* **2017**, *10*, 4927–4933.
- (19) Wang, M.; Wang, M.; Rao, N.; Li, J.; Li, J. Enhancement of CO₂ capture performance of aqueous MEA by mixing with [NH₂-emim][BF₄]. *RSC Adv.* **2018**, *8*, 1987–1992.
- (20) Wu, Y.; Xu, J.; Mumford, K.; Stevens, G. W.; Fei, W.; Wang, Y. Recent advances in carbon dioxide capture and utilization with amines and ionic liquids. *Green Chem. Eng.* **2020**, *1*, 16–32.
- (21) Shohrat, A.; Zhang, M.; Hu, H.; Yang, X.; Liu, L.; Huang, H. Mechanism study on CO₂ capture by ionic liquids made from TFA blended with MEA and MDEA. *Int. J. Greenhouse Gas Control* **2022**, *119*, No. 103709.
- (22) Yuan, S.; Yang, Z.; Ji, X.; Chen, Y.; Sun, Y.; Lu, X. CO₂ Absorption in Mixed Aqueous Solution of MDEA and Cholinium Glycinate. *Energy Fuels* **2017**, *31*, 7325–7333.
- (23) Xiao, M.; Liu, H.; Gao, H.; Olson, W.; Liang, Z. CO₂ capture with hybrid absorbents of low viscosity imidazolium-based ionic liquids and amine. *Appl. Energy* **2019**, *235*, 311–319.
- (24) Hairul, N. A. H.; Shariff, A. M.; Tay, W. H.; Mortel, A. M. A. V. D.; Lau, K. K.; Tan, L. S. Modelling of high pressure CO₂ absorption using PZ plus AMP blended solution in a packed absorption column. *Sep. Purif. Technol.* **2016**, *165*, 179–189.
- (25) Ye, C.; Chen, G.; Yuan, Q. Process Characteristics of CO₂ Absorption by Aqueous Monoethanolamine in a Microchannel Reactor. *Chin. J. Chem. Eng.* **2012**, *20*, 111–119.
- (26) Li, W.; Yang, S.; Guo, X.; He, G.; Jin, H. The effect of operating conditions on acylation of 2-methylnaphthalene in a microchannel reactor. *Chin. J. Chem. Eng.* **2018**, *26*, 1307–1311.
- (27) Ban, Y.; Kikutani, Y.; Tokeshi, M.; Morita, Y. Extraction of Am(III) at the Interface of Organic-Aqueous Two-Layer Flow in a Microchannel. *J. Nucl. Sci. Technol.* **2011**, *48*, 1313–1318.
- (28) Ma, D.; Zhu, C.; Fu, T.; Yuan, X.; Ma, Y. An effective hybrid solvent of MEA/DEEA for CO₂ absorption and its mass transfer performance in microreactor. *Sep. Purif. Technol.* **2020**, *242*, No. 116795.
- (29) Guo, R.; Zhu, C.; Yin, Y.; Fu, T.; Ma, Y. Mass transfer characteristics of CO₂ absorption into 2-amino-2-methyl-1-propanol non-aqueous solution in a microchannel. *J. Ind. Eng. Chem.* **2019**, *75*, 194–201.
- (30) Janati, S.; Aghel, B.; Shadloo, M. S. The effect of alkanolamine mixtures on CO₂ absorption efficiency in T-Shaped microchannel. *Environ. Technol. Innovation* **2021**, *24*, No. 102006.
- (31) Ma, D.; Zhu, C.; Fu, T. T.; Ma, Y.; Yuan, X. Performance and pressure drop of CO₂ absorption into task-specific and halide-free ionic liquids in a microchannel. *AICHE J.* **2022**, *68*, No. e17613.
- (32) Zhang, F.; Zhu, C.; Fu, T.; Jiang, S.; Du, W.; Zhang, Q.; Ma, Y. Mass transfer performance of CO₂ absorption into ionic liquid/ethanol mixture in microchannel. *CIESC J.* **2017**, *68*, 601–611.
- (33) Yin, Y.; Zhu, X.; Zhang, X.; Zhu, C.; Fu, T.; Ma, Y. Mass transfer characteristics of CO₂ absorption in alkanolamine/ionic liquid hybrid aqueous solutions in a microchannel. *CIESC J.* **2022**, *73*, 1930–1939.

- (34) Sun, C.; Wen, S.; Zhao, J.; Zhao, C.; Li, W.; Li, S.; Zhang, D. Mechanism and Kinetics Study of CO₂ Absorption into Blends of N-Methyldiethanolamine and 1-Hydroxyethyl-3-methylimidazolium Glycine Aqueous Solution. *Energy Fuels* **2017**, *31*, 12425–12433.
- (35) Li, W.; Wen, S.; Shen, L.; Zhang, Y.; Sun, C.; Li, S. Mechanism and Kinetic Study of Carbon Dioxide Absorption into a Methyldiethanolamine/1-Hydroxyethyl-3-methylimidazolium Lysine/Water System. *Energy Fuels* **2018**, *32*, 10813–10821.
- (36) Lin, G.; Zhu, C.; Fu, T.; Ma, Y. Mass transfer performance of CO₂ absorption into aqueous mixture of monoethanolamine with N-methyldiethanolamine in microchannel. *CIESC J.* **2018**, *69*, 4675–4682.
- (37) Li, S.; Zhao, C.; Sun, C.; Shi, Y.; Li, W. Reaction Mechanism and Kinetics Study of CO₂ Absorption into [C₂OHmim][Lys]. *Energy Fuels* **2016**, *30*, 8535–8544.
- (38) Ko, J. J.; Li, M. H. Kinetics of absorption of carbon dioxide into solutions of N-methyldiethanolamine plus water. *Chem. Eng. Sci.* **2000**, *55*, 4139–4147.
- (39) Hu, G.; Smith, K. H.; Wu, Y.; Mumford, K. A.; Kentish, S. E.; Stevens, G. W. Carbon dioxide capture by solvent absorption using amino acids: A review. *Chin. J. Chem. Eng.* **2018**, *26*, 2229–2237.
- (40) Yin, Y.; Zhang, X.; Zhu, C.; Fu, T.; Ma, Y. Hydrodynamics and gas-liquid mass transfer in a cross-flow T-junction microchannel: Comparison of two operation modes. *Sep. Purif. Technol.* **2021**, *255*, No. 117697.
- (41) Yao, C.; Yue, J.; Zhao, Y.; Chen, G.; Yuan, Q. Review on flow and mass transfer characteristics of gas-liquid slug flow in microchannels. *CIESC J.* **2015**, *66*, 2759–2766.
- (42) Ma, Y.; Fu, T.; Zhu, C.; Ji, X.; Li, H. Formation mechanism and size prediction of bubble in opposite-flowing T-shaped microchannel. *Trans. Tianjin Univ.* **2010**, *16*, 251–255.
- (43) Jia, H. W.; Zhang, P. Investigation of the Taylor bubble under the effect of dissolution in microchannel. *Chem. Eng. J.* **2016**, *285*, 252–263.
- (44) Haase, S.; Murzin, D. Y.; Salmi, T. Review on hydrodynamics and mass transfer in minichannel wall reactors with gas-liquid Taylor flow. *Chem. Eng. Res. Des.* **2016**, *113*, 304–329.
- (45) Lin, G.; Jiang, S.; Zhu, C.; Fu, T.; Ma, Y. Mass-Transfer Characteristics of CO₂ Absorption into Aqueous Solutions of N-Methyldiethanolamine plus Diethanolamine in a T-Junction Microchannel. *ACS Sustainable Chem. Eng.* **2019**, *7*, 4368–4375.
- (46) Yin, Y.; Fu, T.; Zhu, C.; Guo, R.; Ma, Y.; Li, H. Dynamics and mass transfer characteristics of CO₂ absorption into MEA/[Bmim]⁺[BF₄⁻] aqueous solutions in a microchannel. *Sep. Purif. Technol.* **2019**, *210*, 541–552.
- (47) Yue, J.; Chen, G.; Yuan, Q.; Luo, L.; Gonthier, Y. Hydrodynamics and mass transfer characteristics in gas-liquid flow through a rectangular microchannel. *Chem. Eng. Sci.* **2007**, *62*, 2096–2108.
- (48) Zhou, Z.; Jing, G.; Zhou, L. Characterization and absorption of carbon dioxide into aqueous solution of amino acid ionic liquid [N₁₁₁₁][Gly] and 2-amino-2-methyl-1-propanol. *Chem. Eng. J.* **2012**, *204*–206, 235–243.
- (49) Ji, X. Y.; Ma, Y. G.; Fu, T. T.; Zhu, C. Y.; Wang, D. J. Experimental investigation of the liquid volumetric mass transfer coefficient for upward gas-liquid two-phase flow in rectangular microchannels. *Braz. J. Chem. Eng.* **2010**, *27*, 573–582.
- (50) Ganapathy, H.; Shooshtari, A.; Dessiatoun, S.; Ohadi, M. M.; Alshehhi, M. Hydrodynamics and mass transfer performance of a microreactor for enhanced gas separation processes. *Chem. Eng. J.* **2015**, *266*, 258–270.